Journal of Glaciology

Paper

Cite this article: Yan P, Li Z, Li F, Yang Y, Hao W (2020). Antarctic ice-sheet structures retrieved from P-wave coda autocorrelation method and comparisons with two other single-station passive seismic methods. *Journal of Glaciology* **66**(255), 153–165. https://doi.org/10.1017/jog.2019.95

Received: 9 September 2018
Revised: 20 November 2019
Accepted: 21 November 2019
First published online: 16 December 2019

Key words:
Antarctic glaciology; glacier geophysics; ice-sheet modeling; ice thickness measurements; seismology

Author for correspondence:
Zhiwei Li, E-mail: zwli@whigg.ac.cn;
Fei Li, E-mail: fli@whu.edu.cn

cambridge.org/jog

Antarctic ice-sheet structures retrieved from P-wave coda autocorrelation method and comparisons with two other single-station passive seismic methods

Peng Yan[1], Zhiwei Li[2], Fei Li[1,3], Yuande Yang[1] and Weifeng Hao[1]

[1]Chinese Antarctic Center of Surveying and Mapping, Wuhan University, Wuhan 430079, China; [2]State Key Laboratory of Geodesy and Earth's Dynamics, Institute of Geodesy and Geophysics, Chinese Academy of Sciences, Wuhan 430077, China and [3]State Key Laboratory of Information Engineering in Surveying, Mapping and Remote Sensing, Wuhan University, Wuhan 430079, China

Abstract

Passive seismology is becoming increasingly popular for glacier/ice-sheet structure investigations in Polar regions. Single-station passive seismic methods including P-wave receiver functions (PRFs), horizontal-to-vertical spectral ratio (HVSR) and a recently proposed autocorrelation method have been used to retrieve glacier/ice-sheet structures. Despite their successful applications, analysis regarding their detection abilities in different glaciological environments has not been reported. In this study, we compare ice thicknesses and v_p/v_s ratios obtained from the three methods using data collected at GAMSEIS and POLENET/ANET seismic arrays in Antarctica. Ice thickness estimates derived from the three methods are found to be consistent. Comparisons conducted under various model setups, including those involving tiled layers and sedimentary layers, show that the effectiveness of the autocorrelation method is not superior to the PRF method for retrieving ice-sheet structures. The autocorrelation method however can complement other methods as it only requires a single component seismic record.

1. Introduction

The Antarctic ice sheet covers about 86% of Earth's glacial area (Aster and Winberry, 2017). The seismic structures of the Antarctic ice sheet, including P and S wave velocities (v_p and v_s), v_p/v_s ratios and ice thicknesses, are important parameters of an ice sheet. Accurate seismic velocity structures and thicknesses of the ice sheets provide key constraints to glacial seismicity and subglacial environment studies (Podolskiy and Walter, 2016; Aster and Winberry, 2017). The v_p/v_s ratio, intimately connected to Poisson's ratio, can be used to calculate elastic properties (e.g. bulk modulus and shear modulus) that serve as important parameters in dynamic modeling of ice sheets (Cuffey and Paterson, 2010; Gudmundsson, 2011; Gagliardini and others, 2013; Hanna and others, 2013). Exploring effective methods to investigate ice thickness and elastic properties is therefore of inherent scientific interest. Many geophysical methods, including radio-echo sounding (RES) and active seismic methods, have been applied to investigate ice structures over the past half century (Evans and Robin, 1966; Robinson, 1968; Röthlisberger, 1972; Drewry and others, 1982; Bamber and others, 2001; Gogineni and others, 2001; Lythe and Vaughan, 2001; Kim and others, 2010; Horgan and others, 2011; Fretwell and others, 2013; Li and others, 2013). The RES and active seismic methods both are high-accuracy ice thickness detection methods and are sensitive to density and seismic velocity structures, respectively. They both, however, are relatively laborious and costly to implement in Polar regions.

With the rapid development of portable seismic instrumentation in Polar regions, passive seismic methods can also provide a valuable complement to existing methods for interpreting various kinds of seismic signals related to ice dynamics, as well as for resolving glacier and ice-sheet structures (Podolskiy and Walter, 2016; Aster and Winberry, 2017). Single-station passive seismic methods including P-wave receiver functions (PRFs) and the horizontal-to-vertical spectral ratio (HVSR) provide additional detail of glacier and ice-sheet structures, including ice thickness, ice fabrics and sub-glacial properties. The PRF method applied to teleseismic waveforms, exploiting the converted P-to-S phase and its multiples generated at the interface of a discontinuity, can be used to derive an average depth of the discontinuity and v_p/v_s ratios with the aid of a stacking H-Kappa (v_p/v_s) algorithm (Langston, 1979; Zhu and Kanamori, 2000). The PRF method has been used to investigate ice thicknesses, ice anisotropic structures and subglacial conditions in polar ice sheets (Anandakrishnan and Winberry, 2004; Hansen and others, 2010; Wittlinger and Farra, 2012, 2015; Chaput and others, 2014; Walter and others, 2014; Yan and others, 2017). By computing the ratio between the horizontal and vertical Fourier spectra of three-component ambient seismic noise or an earthquake record, the HVSR method can quickly retrieve the seismic structures of a medium (Nakamura, 1989; Lunedei and Malischewsky, 2015; Bao and others, 2018). This method has been increasingly applied in ice environments to study seismic structures of uppermost

permafrost, firn, glaciers and ice sheets (Lévêque and others, 2010; Picotti and others, 2017; Yan and others, 2018; Köhler and Weidle, 2019). More recently, Preiswerk and others (2019) have illustrated the effect of geometry of different types of Alpine glaciers on the seismic wavefield and consequently on the retrieved glacier structures using the HVSR method.

Some other passive seismic methods including ambient noise interference and shear wave splitting methods have also be used to estimate seismic structures of ice sheets effectively. Zhan and others (2014) detected the seismic resonances within the sub-ice water cavity of Amery Ice Shelf using ambient seismic noise cross-correlations. Walter and others (2015) measured phase velocities using ambient seismicity on glaciers and ice sheets. Diez and others (2016) investigated the associated firn/ice/water structure of Ross Ice Shelf with surface-wave dispersion curves. Moreover, the seismic anisotropic structure of ice sheets can also be revealed by passive seismic methods. Harland and others (2013) measured ice anisotropy in Rutford Ice Stream, Antarctica with basal seismicity using the shear-wave splitting method. With more data involved, Smith and others (2017) observed the diffuse horizontal partial girdle fabric in Rutford Ice Stream, which is different from the anisotropic cluster fabric found in other ice streams such as Whillans Ice Stream (Picotti and others, 2015).

Though these results are encouraging, it is still valuable to explore ways to expand the toolbox for glacier and ice-sheet structure detection. Phạm and Tkalčić (2017) have proposed a telesismic p-wave coda autocorrelation method, which only uses a single component of seismic records to recover the reflection response from a shallow discontinuity interface (i.e. an ice-bedrock interface). The autocorrelation method together with PRF and HVSR methods that can be applied to ice-sheet structure investigations is all single-station passive seismic methods. The detection abilities of the three methods for retrieving ice-sheet structures in different glacialogical environments such as tilted interfaces and different ice-sediment-bedrock settings have not been analyzed. In this study, the seismic structures, including v_p/v_s ratios and thicknesses of ice sheets are retrieved beneath 41 stations in East and West Antarctica generally following the autocorrelation method proposed by Phạm and Tkalčić (2017). Given that an improved autocorrelation method was also recently applied to a similar set of stations, as in this study (Phạm and Tkalčić, 2018), we have compared results for stations common to both studies. The consistency of results obtained from independent studies validates the effectiveness of the autocorrelation method. Moreover, comparisons of PRF, HVSR and the autocorrelation methods with their general theories, observed results and theoretical simulations will also be presented in this study.

2. Data and methods

To compare results obtained using PRF, HVSR and autocorrelation methods, we collected data from stations that were commonly processed using PRF and HVSR methods in our previous studies (Yan and others, 2017, 2018). Specifically, we used data that were recorded by GAMSEIS, and POLENET/ANET seismic arrays that efficiently cover East and West Antarctica (Fig. 1). The criteria for selecting teleseismic events for the autocorrelation technique were generally the same as those in the PRF method; the epicentral azimuth was set between 30 and 90°; at a magnitude greater than 5.5. In total, we picked 978 teleseismic events using this standard from the GAMSEIS and ANET seismic arrays, respectively, during the year 2009 and from 2010 to 2011 (Fig. S1).

The autocorrelation technique is a seismic interference method for passive seismic imaging which exploits a fast correlation algorithm. The technique was first proposed by Claerbout (1968) in a layered acoustic medium. He demonstrated that the autocorrelation of the transmission response of a seismogram generated with a source at depth corresponds to the reflection response of a co-located source and receiver at the surface (Figs 2b and c). This method was extended to a 1-D elastic medium by Frasier (1970) and later to a 3-D elastic medium by Wapenaar and others (2004). Unlike cross-correlations conducted to retrieve Green's function between station pairs, and often used to extract the surface-wave component (Campillo and Paul, 2003; Shapiro and Campillo, 2004; Li and others, 2016), the autocorrelation method can retrieve body-wave reflection responses of discontinuities at different depths by assuming a co-located source and receiver at a single station. Compared with the PRF method that exploits a deconvolution algorithm between radial (or tangential) and vertical components, and the HVSR method that divides vertical and horizontal amplitude spectra, the autocorrelation method uses only one component employing the correlation algorithm.

The autocorrelation method has shown its effectiveness when imaging interfaces associated with strong seismic impedance contrasts in Earth crust and upper mantle (e.g. Moho and lithosphere asthenosphere boundary, and the basement of sedimentary basins) (Tibuleac and others, 2012; Gorbatov and others, 2012; Kennett, 2015; Kennett and others, 2015; Saygin and others, 2017) and seismic interfaces on the moon (Nishitsuji and others, 2016). In most previous studies, the autocorrelation method is applied to ambient noise data. When applied to ambient noise data, a large amount of noise data is required to enhance the signal-to-noise ratio (SNR) and the stability of results. The autocorrelation technique applied to teleseismic events has recently been validated as effective for mapping reflection responses of interfaces at both deep and shallow depths (Sun and Kennett, 2016, 2017; Phạm and Tkalčić, 2017). The use of teleseismic events has advantages, including less-strict requirements for data volume and processing procedures that are simpler than those required with ambient noise data.

Processing procedures in the autocorrelation method generally include pre-processing, such as data-quality control and whitening, autocorrelation in time or frequency domains and post-processing such as filtering and stacking. In this study, we computed autocorrelograms in the frequency domain, which is more efficient than processing in the time domain (since a deconvolution procedure required in the time domain is equivalent to a simple division in the frequency domain). Pre-processing procedures were conducted including the removal of the mean and linear trend. A whiten operation was applied to the pre-processed waveforms so as to enhance the high frequency signals that attenuated when propagating along the ray path. In contrast to Phạm and Tkalčić (2018), which improved the autocorrelation method by using a station-specific tuning whiten width, we adopted a fixed one in this procedure and achieved similar results. The adoption of a fixed whiten width is more suitable for automatic processing, especially for seismic arrays. Autocorrelograms were calculated in the frequency domain, and the positive time lags of a symmetric autocorrelogram were retained. A cosine taper function was applied to remove the inherent zero-time peak in the retained autocorrelogram. To recover coherent reflection responses of the ice-sheet-rock interface in both vertical and radial components, several sets of Butterworth bandpass filters were tested on the retained autocorrelogram. A final 0.5–2 Hz frequency band was adopted as it presented the clearest reflection responses (Fig. S2). Retained time series data were normalized using the maximum amplitude. To enhance the reflection response from the ice-bedrock interface, the autocorrelograms of all teleseismic events recorded at one station were stacked using the time-frequency domain phase weighted stacking (TF-PWS) technique (Schimmel and Gallart, 2007). Following a

https://doi.org/10.1017/jog.2019.95 Published online by Cambridge University Press

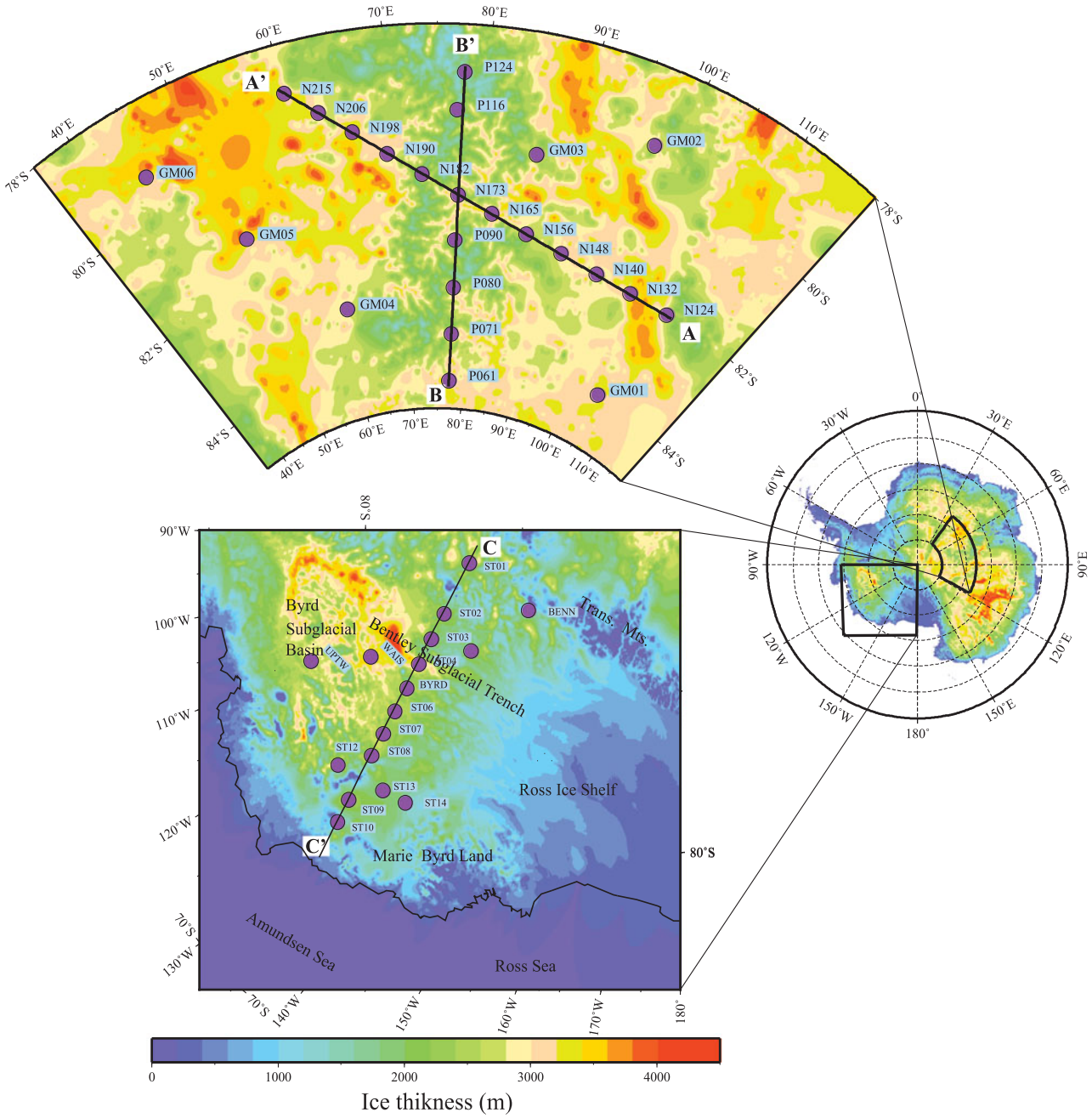

Fig. 1. Station distribution of the two seismic arrays used in this study. Some stations are aligned in three transects marked with AA′, BB′ and CC′. Ice thickness data are from the Bedmap2 dataset (Fretwell and others, 2013).

previous study, the PWS order that we adopted in the stacking procedure is 2 (Pham and Tkalčić, 2017).

Theoretical autocorrelograms using synthetic teleseismic waveforms were also calculated to validate the observed autocorrelograms for each station. The synthetic teleseismic waveforms were computed via convolution of a source time function and an impulse response of a local structure (Fig. 3a). Unlike the source time function adopted by Pham and Tkalčić (2017), which is comprised of an array of normally distributed random numbers with mean 0 and Std dev. 1 (Fig. 3b), we use 100 real teleseismic waveforms in the vertical component, each lasting 12 s to represent the real source time function (Fig. 3c). The use of a real vertical teleseismic waveform as a source time function has advantages over that adopted by Pham and Tkalčić (2017) as it uses the real source and involves the effect of ray paths, making the synthetic teleseismic waveforms more similar to the real ones. The local structure impulse response was calculated using the reflection program (repknt, Randall, 1989), assuming a homogeneous and isotropic ice-sheet layer atop hard bedrock. The parameters including ice thickness and P and S wave velocities used in models to generate local impulses are derived from the Bedmap2 dataset and previous studies (Hansen and others, 2010; Wittlinger and Farra, 2012; Ramirez and others, 2016). Given that the thickness of ice sheets is much thinner, <4 km, than that of crustal and mantle discontinuities, the reflection delay times of the ice-bedrock interfaces are independent of ray parameters (Pham and Tkalčić, 2017). We therefore calculated the local impulse responses at fixed slowness, 0.06 s km^{-1}, for the P wave, and 0.12 s km^{-1}, for the S wave (Sun and Kennett, 2016) (Figs 3f and g). The subsequent processing procedures to generate theoretical autocorrelograms using synthetic teleseismic waveforms remain the same as those applied to real teleseismic P wave coda waveforms.

https://doi.org/10.1017/jog.2019.95 Published online by Cambridge University Press

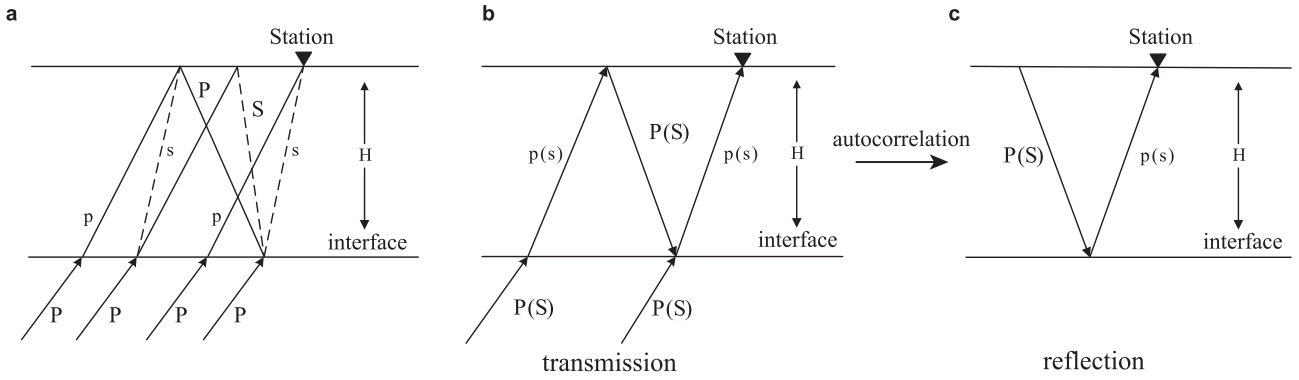

Fig. 2. Sketch of teleseismic phases to compare the PRF and autocorrelation methods. Panel (a) presents the direct P wave, the converted Ps wave and the multiples traveling through an ice-sheet layer used in the PRF method. Panel (b) shows P or S transmissions, while panel (c) shows P or S reflections (modified after Gorbatov and others, 2012). When applied with the autocorrelation technique, the transmitted P wave or S wave is equivalent to reflection waves generated using a co-located source and receiver.

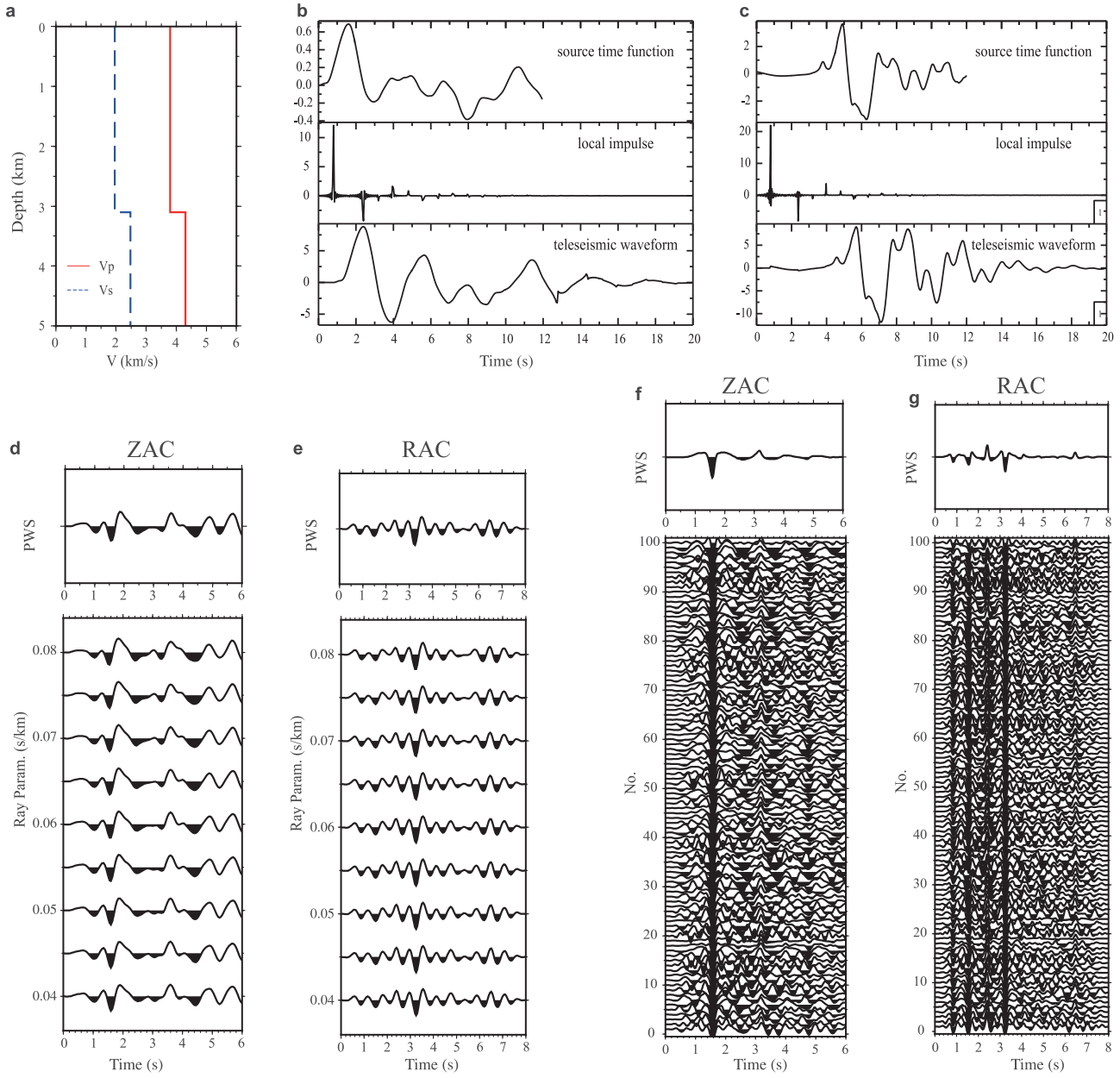

Fig. 3. Example of synthetic teleseismic waveforms generated using different source time functions and the radial and the vertical autocorrelograms before and after TF-PWS stacking for station GM01. Panel (a), v_p and v_s profiles for station GM01 with a 3.1 km thick ice layer. Panel (b), from top to bottom: a source time function similar to that adopted by Pham and Tkalčić (2017), is comprised of an array of normally distributed random numbers with mean 0 and Std dev. 1, a local structure impulse response, a complete teleseismic waveform. Panel (c), the same as panel (b) except the source time function is a segment of a real vertical teleseismic waveform. Panels (d) and (e), the synthetic vertical and radial autocorrelograms generated using the source time function shown in panel (b). Panels (f) and (g), the synthetic vertical and radial autocorrelograms generated using 100 source time functions as shown in panel (c).

https://doi.org/10.1017/jog.2019.95 Published online by Cambridge University Press

3. Results

High quality vertical autocorrelograms were obtained for all 41 stations; 39 were obtained for the radial component, because there were no clear reflection responses or too few high quality autocorrelograms at stations ST04 and ST06 (Fig. S3). The stacked autocorrelograms in both the vertical and the radial components for the 39 stations are displayed in Fig. 4. Comparisons of the autocorrelograms before and after stacking show that the PWS technique enhances the coherent phases and suppresses incoherent phases, thus improving the SNR of the autocorrelograms.

As shown in Figs. 4a and b, there are clear dominant and negative peaks for each autocorrelogram in both the vertical and the radial components. The arrival times show significant variations between different stations, reflecting the variations of ice thicknesses beneath these stations. An examination of the arrival times of the negative peaks in the vertical component reveals that peaks appear in the 0.80–1.68 s range, while the arrival times of the radial peaks are approximately double those for the vertical peaks (i.e. 1.60–3.40 s). The negative peaks are the first P or S reflection responses of the ice-bedrock interface. The first reflection responses show negative polarities because the first reflection experiences a single phase flip due to a single reflection of the free surface (Pham and Tkalčić, 2017). Moreover, clear positive peaks appear at twice the time of the first P (S) reflection responses for most stations, which are certainly the second reflections. These peaks show positive polarities because they experience twice the free surface reflections, thus their travel times are generally double those of the first reflections. The second reflection responses are generally much weaker or even invisible for some stations (e.g. N148, GM03 and ST10) because the seismic energy attenuates during subsequent propagation in ice. We then define the arrival times for the P and S waves (t_p and t_s) to be the times at which the peaks of the maximum amplitudes occur. The chosen arrival times are associated with uncertainties that arise from the TF-PWS stacking and the maximum amplitude identification. In this sense, we estimate the uncertainties (δt_p and δt_s) using the difference in arrival times between the peak amplitude and $\sqrt{2}/2$ times the peak amplitude. The P and the S wave arrival times, as well as their associated uncertainties are listed in Table 1.

Having identified the arrival times of P and S wave reflection responses, we calculate the value of the v_p/v_s ratio for each station. The v_p/v_s ratio is proportional to the ratio between the S and the P wave arrival times as their ray paths are both near vertical traveling through the ice sheet; that is

$$\frac{v_p}{v_s} = \frac{t_s}{t_p} \tag{1}$$

where t_p and t_s are the arrival times of P and S wave reflection responses, respectively. Using the uncertainties of the P and the S wave arrival times, we calculate the errors of the v_p/v_s ratios

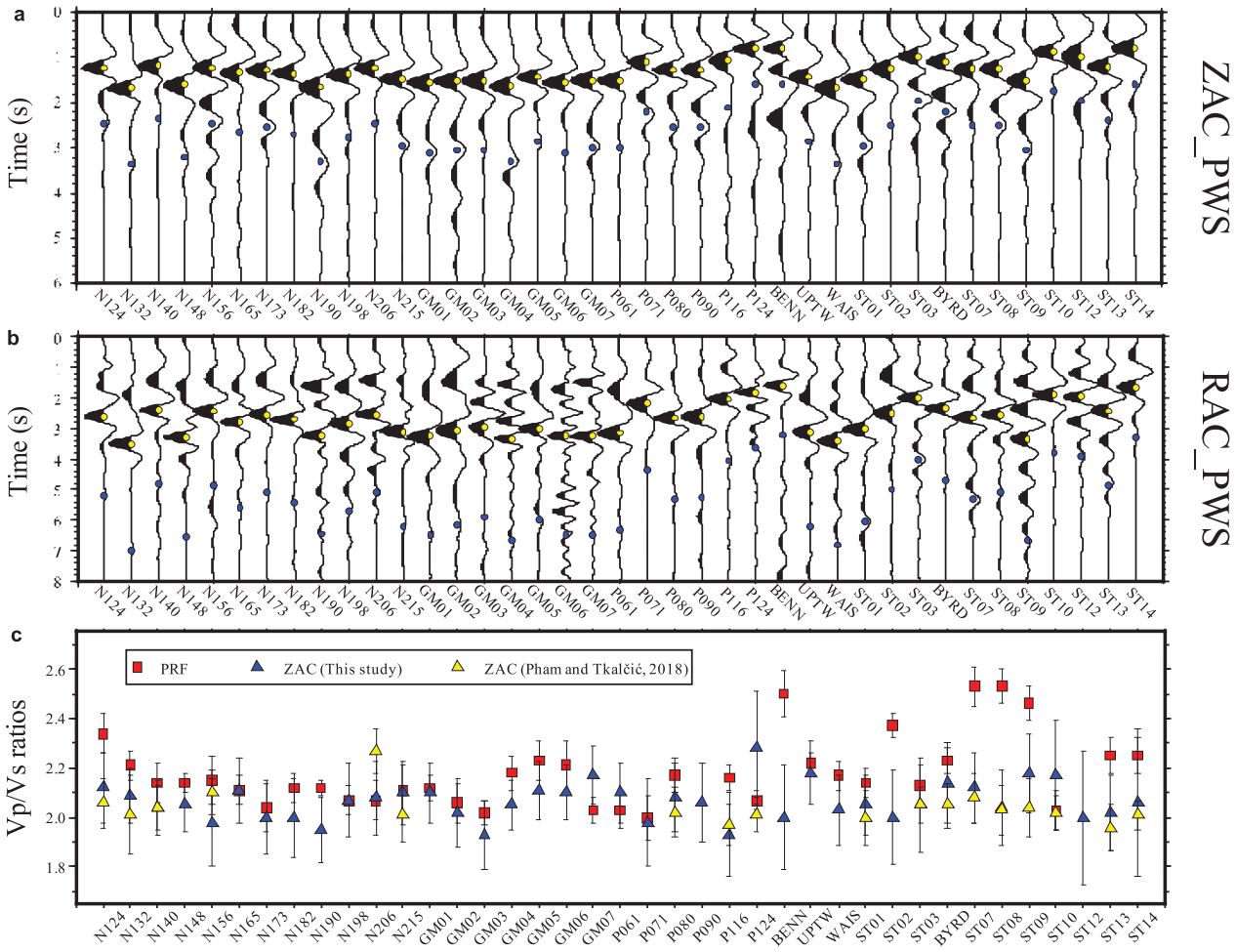

Fig. 4. Stacked radial and vertical autocorrelograms of 39 stations. Panel (a), the stacked vertical autocorrelograms (ZAC). Yellow circles represent the arrival times of P wave reflection responses, and blue circles denote arrival times that double the values of the first P wave reflection arrival times. Panel (b), the same as panel (a), but for the radial autocorrelograms and S wave reflection responses. Panel (c), v_p/v_s ratio values derived from the ratios of S wave and P wave reflections obtained from this study and Pham and Tkalčić (2018). The v_p/v_s ratio estimates obtained from the PRF method are also shown in panel (c) (Yan and others, 2017).

https://doi.org/10.1017/jog.2019.95 Published online by Cambridge University Press

Table 1. Arrival times of the reflection responses for the P and S waves, and the calculated v_p/v_s and Poisson's ratios

Station	t_p[a] (s)	t_s[a] (s)	v_p/v_s ratios	Poisson's ratios[b]	Station	t_p (s)	t_s (s)	v_p/v_s ratios	Poisson's ratios
N124	1.23 ± 0.08	2.60 ± 0.08	2.12 ± 0.14	0.36	P071	1.10 ± 0.08	2.18 ± 0.13	1.98 + 0.18	0.33
N132	1.68 ± 0.08	3.50 ± 0.10	2.09 ± 0.11	0.35	P080	1.28 ± 0.08	2.65 ± 0.07	2.08 + 0.14	0.35
N140	1.18 ± 0.05	2.40 ± 0.07	2.04 ± 0.11	0.34	P090	1.28 ± 0.08	2.63 ± 0.13	2.06 + 0.16	0.35
N148	1.60 ± 0.08	3.28 ± 0.07	2.05 ± 0.11	0.34	P116	1.05 ± 0.08	2.03 ± 0.10	1.93 + 0.17	0.32
N156	1.23 ± 0.10	2.43 ± 0.10	1.98 ± 0.18	0.33	P124	0.80 ± 0.08	1.83 ± 0.08	2.28 + 0.23	0.38
N165	1.33 ± 0.08	2.80 ± 0.07	2.11 ± 0.13	0.36	BENN	0.80 ± 0.08	1.60 ± 0.08	2.00 + 0.21	0.33
N173	1.28 ± 0.08	2.55 ± 0.13	2.00 ± 0.15	0.33	BYRD	1.10 ± 0.08	2.35 ± 0.08	2.14 + 0.16	0.36
N182	1.35 ± 0.10	2.70 ± 0.08	2.00 ± 0.16	0.33	ST01	1.48 ± 0.10	3.03 ± 0.10	2.05 + 0.12	0.34
N190	1.65 ± 0.10	3.23 ± 0.08	1.95 ± 0.13	0.32	ST02	1.25 ± 0.08	2.50 ± 0.13	2.00 + 0.19	0.33
N198	1.38 ± 0.08	2.85 ± 0.13	2.07 ± 0.15	0.35	ST03	0.98 ± 0.10	2.00 ± 0.10	2.05 + 0.19	0.34
N206	1.23 ± 0.08	2.55 ± 0.10	2.08 ± 0.15	0.35	ST07	1.25 ± 0.08	2.65 ± 0.07	2.12 + 0.14	0.36
N215	1.48 ± 0.08	3.10 ± 0.10	2.10 ± 0.13	0.35	ST08	1.25 ± 0.08	2.55 ± 0.10	2.04 + 0.15	0.34
GM01	1.55 ± 0.08	3.25 ± 0.10	2.10 ± 0.12	0.35	ST09	1.53 ± 0.08	3.33 ± 0.10	2.18 + 0.16	0.37
GM02	1.53 ± 0.08	3.08 ± 0.15	2.02 ± 0.14	0.34	ST10	0.88 ± 0.08	1.90 ± 0.10	2.17 + 0.22	0.37
GM03	1.53 ± 0.10	2.95 ± 0.10	1.93 ± 0.14	0.32	ST12	0.98 ± 0.10	1.95 ± 0.08	2.00 + 0.27	0.33
GM04	1.63 ± 0.08	3.33 ± 0.05	2.05 ± 0.10	0.34	ST13	1.20 ± 0.08	2.43 ± 0.10	2.02 + 0.15	0.34
GM05	1.43 ± 0.08	3.00 ± 0.08	2.11 ± 0.12	0.35	ST14	0.80 ± 0.13	1.65 ± 0.13	2.06 + 0.30	0.35
GM06	1.55 ± 0.08	3.25 ± 0.08	2.10 ± 0.11	0.35	UPTW	1.43 ± 0.08	3.10 ± 0.10	2.18 + 0.13	0.37
GM07	1.50 ± 0.08	3.25 ± 0.08	2.17 ± 0.12	0.36	WAIS	1.68 ± 0.10	3.4 ± 0.13	2.03 + 0.14	0.34
P061	1.50 ± 0.08	3.15 ± 0.10	2.10 ± 0.12	0.35					

[a]The uncertainty of the arrival times for the P and the S waves is estimated using the difference in the arrival times between the peak amplitude and $\sqrt{2}/2$ times the peak amplitude.
[b]$\upsilon = \frac{(v_p/v_s)^2 - 2}{2(v_p/v_s)^2 - 2}$

from the error propagation law

$$\delta\frac{v_p}{v_s} = \sqrt{\frac{\delta t_s^2}{t_p^2} + \frac{t_s^2}{t_p^4}\delta t_p^2} \quad (2)$$

where δt_p and δt_s are uncertainties calculated using the difference in the arrival times between the peak amplitude and $\sqrt{2}/2$ times the peak amplitude. As shown in Fig. 4c, the values of v_p/v_s ratios are generally in the range of 1.95–2.20 for most stations (Table 1). The minimum and the maximum values of the v_p/v_s ratios are 1.93 for GM03 and P116 stations and 2.28 for P124 station, respectively. The average value of v_p/v_s ratios for the 39 stations is 2.07. The results are consistent with the values deduced from laboratory measurements of v_p and v_s in a single ice crystal; i.e. the values of v_p/v_s ratios along and perpendicular to the *c*-axis direction are respectively, 2.14 and 1.97 (Gagnon and others, 1988).

In addition, the ice-bedrock depths (ice thicknesses) can also be computed using the reflection arrival time and the corresponding seismic velocity of a particular component (vertical or radial). Given that the quality of the vertical autocorrelograms is better than that of the radial ones (there are phase-interfering S wave reflection responses in radial autocorrelograms as shown in Fig. 4b), we use the velocity and reflection arrival times in the vertical component to calculate the ice thickness; that is,

$$H = \frac{v_p t_p}{2} \quad (3)$$

Neglecting the variations of ice parameters at different sites, a homogeneous v_p value (3800 m s^{-1}) was adopted in our study, which was determined using a reflection seismic method and was widely used in relevant studies (Robinson, 1968; Röthlisberger, 1972). The uncertainty of P wave velocity (δv_p) is set to 100 m s^{-1} considering the influence of temperature and anisotropy on ice elastic properties (Kohnen, 1974). Errors from the picked arrival time of the P wave reflection response and from the P wave velocity both contribute to the uncertainty of the estimated ice thickness. Note that the calculated ice thickness would be slightly larger than the 'ground truth' ice thickness as the P wave velocity in the uncompacted firn near the surface is smaller than that in the deeper ice (the associated error however can be neglected as the seismic velocity quickly reaches 3800 m s^{-1}, Robinson, 1968; Röthlisberger, 1972). Hereafter we define the ice thickness estimates obtained from the autocorrelograms using the P reflection responses as ZAC estimates. The computed ice thicknesses and the associated uncertainties (Eqn (4)) are listed in Table S1.

$$\delta H = \frac{\sqrt{v_p^2\delta t_p^2 + t_p^2\delta v_p^2}}{2} \quad (4)$$

4. Discussion

The stacked theoretical autocorrelograms together with the Bedmap2 ice thickness variations across three profiles are shown in Figs 5 and S5. There is good agreement between the observed and the theoretical arrivals of the reflection responses for most stations. The relative errors of the observed first P wave reflections to the theoretical ones are within 5, 10 and 15% at a total of 19, 27 and 32 stations, respectively. Similarly, the relative errors for S wave reflections for 17, 27 and 29 stations are within 5, 10 and 15% threshold, respectively. In addition, the variations between the Bedmap2 ice thicknesses and the reflection arrivals for stations along the three profiles are closely correlated. Given that the Bedmap2 ice thicknesses adopted to generate theoretical teleseismic waveforms are associated with certain uncertainties at these stations (Fretwell and others, 2013; Yan and others, 2018), we can conclude that the autocorrelation method can effectively image both the P wave and the S wave reflection responses of the ice-bedrock interface.

Given the lack of 'ground truth' ice thickness from direct measurement methods such as drillings, calculated ice thickness is validated by comparing the ZAC estimate with the corresponding Bedmap2 ice thickness at each site. Differences between the ZAC estimates and the Bedmap2 ice thickness are within 100, 200, 300 and 400 m for 15, 24, 29 and 33 stations, respectively. The relative errors of the ZAC estimates to the Bedmap2 ice thickness are the same as those of the observed arrival times to the theoretical arrival times because the same v_p value is used in calculations of ice thicknesses and models to generate theoretical

https://doi.org/10.1017/jog.2019.95 Published online by Cambridge University Press

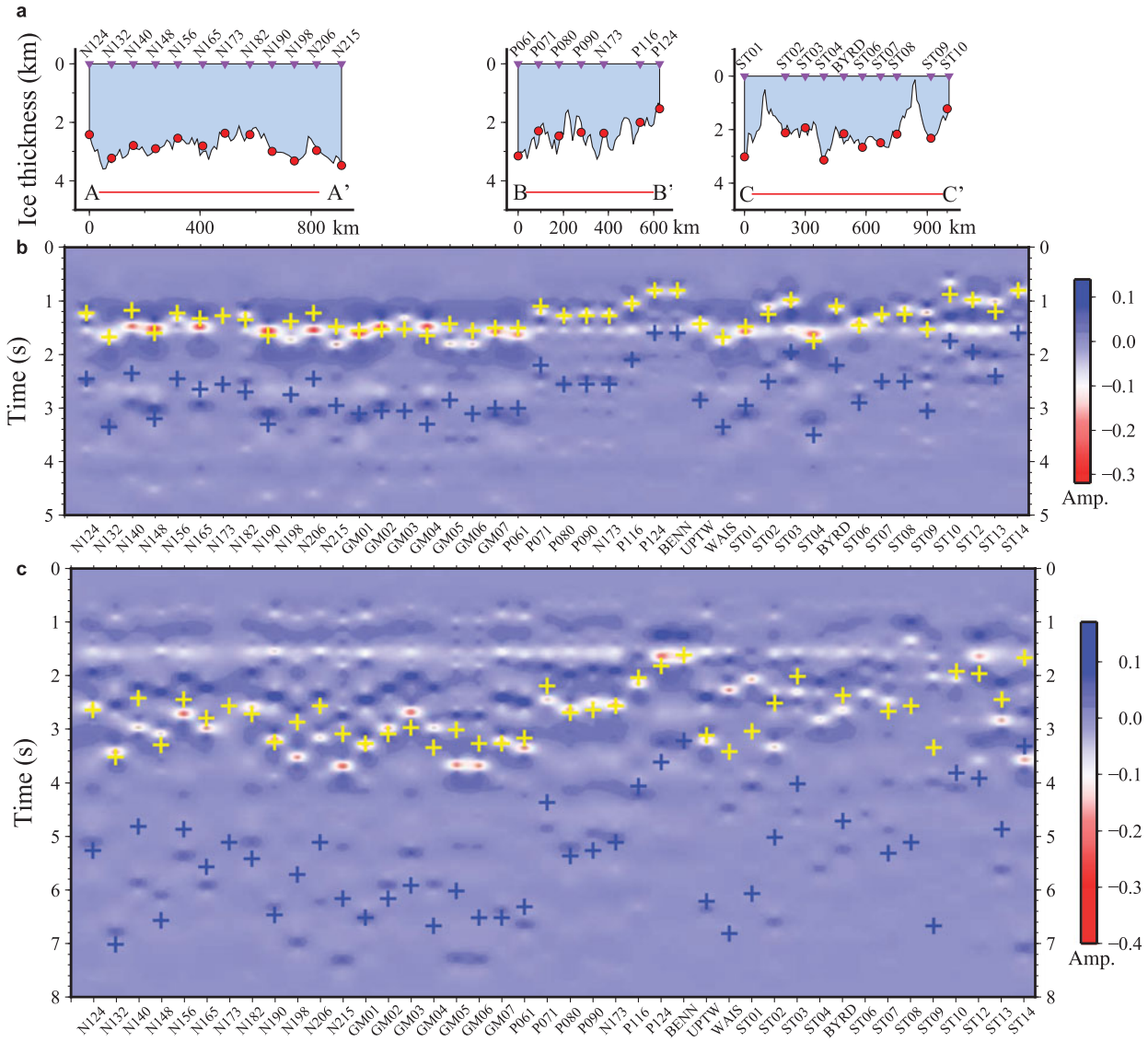

Fig. 5. Synthetic stacked radial and vertical autocorrelograms for each station. Panel (a) shows Bedmap2 ice thickness variations along the three profiles and the reference thicknesses (red dots) used to build models. Panel (b) displays synthetic vertical autocorrelograms. Yellow and blue crosses denote the arrival times of the observed first and second P wave reflection responses (corresponding to the yellow and blue circles shown in Fig. 4a). Panel (c) is similar to panel (b), but for radial autocorrelograms. Model parameters used to generate theoretical teleseismic waveforms are comprised of Bedmap2 ice thickness, v_p and v_s values. v_p is set to 3800 m s^{-1} referring to previous studies and v_s is deduced from the relationship between v_p and v_p/v_s ratio.

autocorrelograms. Our estimates show a good agreement with results obtained from Pham and Tkalčić (2018), which investigated Antarctic ice-sheet properties using an autocorrelation method with an improved scheme of selecting the spectral whiten width. Comparison shows, for the 19, 27 and 33 out of 38 stations that exhibit clear P wave reflections in both studies, the relative errors are within 5, 10 and 15%, respectively (Fig. 6). Note that instead of using ice thickness results estimated by Pham and Tkalčić (2018) directly, we adopt their P wave arrival times and use the same P wave velocity value as in our study to calculate ice thicknesses since different v_p values were used in two studies. Though the relative errors of ice thickness at stations P061 and N190 appear over 50% (Fig. 6), we find that the arrival times are shown in autocorrelograms in Pham and Tkalčić (2018) and our studies are in fact very close. The differences are caused by their recording mistakes as the arrival time values recorded in the table are not consistent with the ones shown in the autocorrelograms (Pham and Tkalčić, 2018).

As no comparison among ice thickness estimates obtained from the PRF, HVSR and autocorrelation methods has been conducted before, we compared the ZAC estimates with results derived from the PRF and HVSR methods in our previous studies (Yan and others, 2017, 2018). We have calculated the average ice thickness at the 35 stations that successfully acquire ice thickness estimates using the PRF, HVSR and autocorrelation methods simultaneously. It shows that the ice thickness estimates obtained from the three methods are consistent as the differences of ice thickness values estimated by each method from the average of their ice thickness values are within 200 m at ~30 stations. Table S2 displays the relative errors of the ice thickness estimates with respect to the Bedmap2 ice thickness. We find that the level of relative error in the estimates is also consistent – the relative errors are within 15% for 25 stations, including GM01, P061, BYRD and ST01. This consistency can also be found for the seven stations with relatively large relative errors to the Bedmap2 ice thicknesses (over 15%), such as the N206, GM03 and ST09 stations. Similar disagreements with Bedmap2 ice thicknesses at these stations have also been found by Pham and Tkalčić (2018).

It is possible that the relatively large deviations from Bedmap2 ice thicknesses at the seven stations could be attributed to

https://doi.org/10.1017/jog.2019.95 Published online by Cambridge University Press

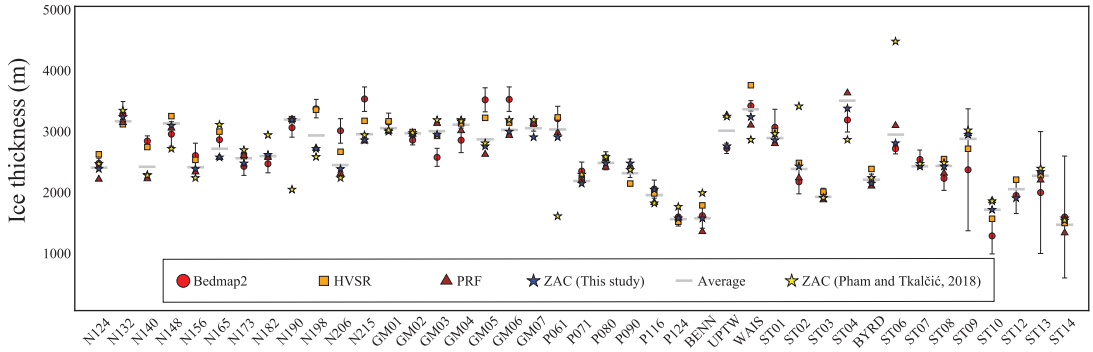

Fig. 6. Comparison of the ZAC ice thickness estimates with results obtained using the HVSR and PRF methods in our previous studies (Yan and others, 2017, 2018). The grey horizontal line in the plot indicates the average ice thickness of the HVSR, PRF and ZAC (this study) estimates for each station. The red circle and its bar represent the Bedmap2 ice thickness and its associated uncertainty for each station (Fretwell and others, 2013). The ZAC estimates measured by Pham and Tkalčić (ZAC) are also displayed here (yellow stars) (note that the thickness values are a product of P wave arrival times taken from Pham and Tkalčić (2018) and v_p adopted in this study; we don't use their ice thickness values as two slightly different v_p values are used in different studies).

uncertainties in Bedmap2 ice thicknesses. More accurate ice thicknesses could be required to validate these specific results. The deviations could also be caused by the complex subglacial settings beneath these stations. As pointed out by Chaput and others (2014), it is difficult to model the converted phases from the base of the ice sheet in their PRF study for a few stations including ST04, ST06 and ST09, which could possibly be influenced by anisotropy or basal dip structures. Therefore, we calculated autocorrelograms using synthetic teleseismic waveforms derived from models assuming an ice-sheet layer atop an inclined bedrock layer with dip angles varying from 5 to 30°, to show the effect of nonplanar basal topography on autocorrelograms. Figure S6 shows the theoretical teleseismic waveforms with a range of back azimuths between 0 and 360° generated using the raysum codes (Frederiksen and Bostock, 2000). Figure S7 displays the resulting autocorrelograms obtained using the theoretical teleseismic waveforms with the processing strategies mentioned in section 2. We can find that the autocorrelation reflections from different back azimuths show clear variations in values of amplitudes and arrival times. Such features become more remarkable as the dip angle increases. For example, the arrival time of the vertical autocorrelation reflections shown in the left panel of Fig. S7 decreases from 1.55 to 1.40 s when the dip angle increases from 5 to 15°. In addition to decreasing arrival times, the autocorrelations become more complex when the dip angle exceeds 20°. The same characteristics can also be found in radial autocorrelograms. With the PWS technique applied, we found that the azimuthal effect on the autocorrelograms resulting from the inclined basal structures is suppressed as a consistent autocorrelation reflection from different back azimuths is obtained (Fig. S8). Arrival times identified from the consistent autocorrelograms only reflect an average ice thickness beneath a station. Therefore, basal dips could certainly affect the arrival times of P and S wave reflection responses and consequently lead to errors of ice thickness estimates (and v_p/v_s ratios).

The PRF and the autocorrelation methods share certain similarities in data selection criteria and in the underlying equations in the frequency domain

$$ZAC(w) = P^*(\omega)P(\omega) \tag{5}$$

$$PRF(\omega) = \frac{P^*(\omega)S(\omega)}{\max\{P^*(\omega)P(\omega),\ \ c \cdot P^*_{\max}P_{\max}\}} \tag{6}$$

where $P(\omega)$ and $S(\omega)$ are the vertical and radial component spectra from teleseisms at angular frequency ω, and $P^*(\omega)$ is the complex conjugation of $P(\omega)$ (Sun and Kennett, 2016). The water level parameter c in Eqn (6) is used to avoid division by very small numbers by reducing the magnitude of the trough in the vertical component spectrum (Clayton and Wiggins, 1976). For small c, Eqn (6) approaches deconvolution, while it approaches a scaled cross-correlation as c becomes large. Considering the similarities of the PRF and autocorrelation methods, we compare their results for ice thickness and v_p/v_s ratios. It turns out that ice thickness estimates obtained from the PRF and autocorrelation methods are closely matched (for the total of 38 stations that are common to both methods, the relative error of the ZAC estimates to the PRF estimates for 22 and 34 station are less than 5 and 10%, respectively). Taking the uncertainties in the estimated v_p/v_s ratios into account, the values of v_p/v_s ratios determined using PRF and autocorrelation methods are generally consistent and ~2.00 for most stations (see Fig 4c). The differences are less than 0.1 for 17 stations, while the differences for stations such as BENN, ST02, ST07 and ST08 exceed 0.35. Further analysis indicates that the quality of PRF waveforms used to conduct H-Kappa stacking (Zhu and Kanamori, 2000) for the four stations is poorer than that of the autocorrelograms (Fig. S4). As is commonly acknowledged, the inherent trade-off between the thickness and shear-wave velocity for the PRF method also contributes to uncertainties in the v_p/v_s estimates.

To clearly show the capacity of the two methods for detecting ice properties, we have built a set of models (Fig. S10) to compare results obtained from both PRF and autocorrelation methods (Anandakrishnan and Winberry, 2004; Chaput and others, 2014). Conclusions can be drawn by comparing results using different pairs of models (Figs 7, 8 and S11–S13). Table S1 displays the theoretical arrival times of P and S wave reflection responses calculated from model parameters (Eqns (7–9)), as well as the observed arrival times derived from the synthetic autocorrelograms using a bootstrapping technique (Fig. S14).

$$t^{\text{ice}}_{\text{p(s)}} = \frac{2H_{\text{ice}}}{v_{\text{p(s)}}} \tag{7}$$

$$t^{\text{ice+sed}}_{\text{p(s)}} = \frac{2(H_{\text{ice}} + H_{\text{sed}})}{\bar{v}_{\text{p(s)}}} \tag{8}$$

$$\bar{v}_{\text{p(s)}} = \frac{(H_{\text{ice}} + H_{\text{sed}})v^{\text{ice}}_{\text{p(s)}}v^{\text{sed}}_{\text{p(s)}}}{H_{\text{ice}}v^{\text{sed}}_{\text{p(s)}} + H_{\text{sed}}v^{\text{ice}}_{\text{p(s)}}} \tag{9}$$

where H_{ice} and H_{sed} are ice and sediment thicknesses, and $t^{\text{ice}}_{\text{p(s)}}$, $t^{\text{ice+sed}}_{\text{p(s)}}$ are the theoretical arrival times of P (S) wave reflection

https://doi.org/10.1017/jog.2019.95 Published online by Cambridge University Press

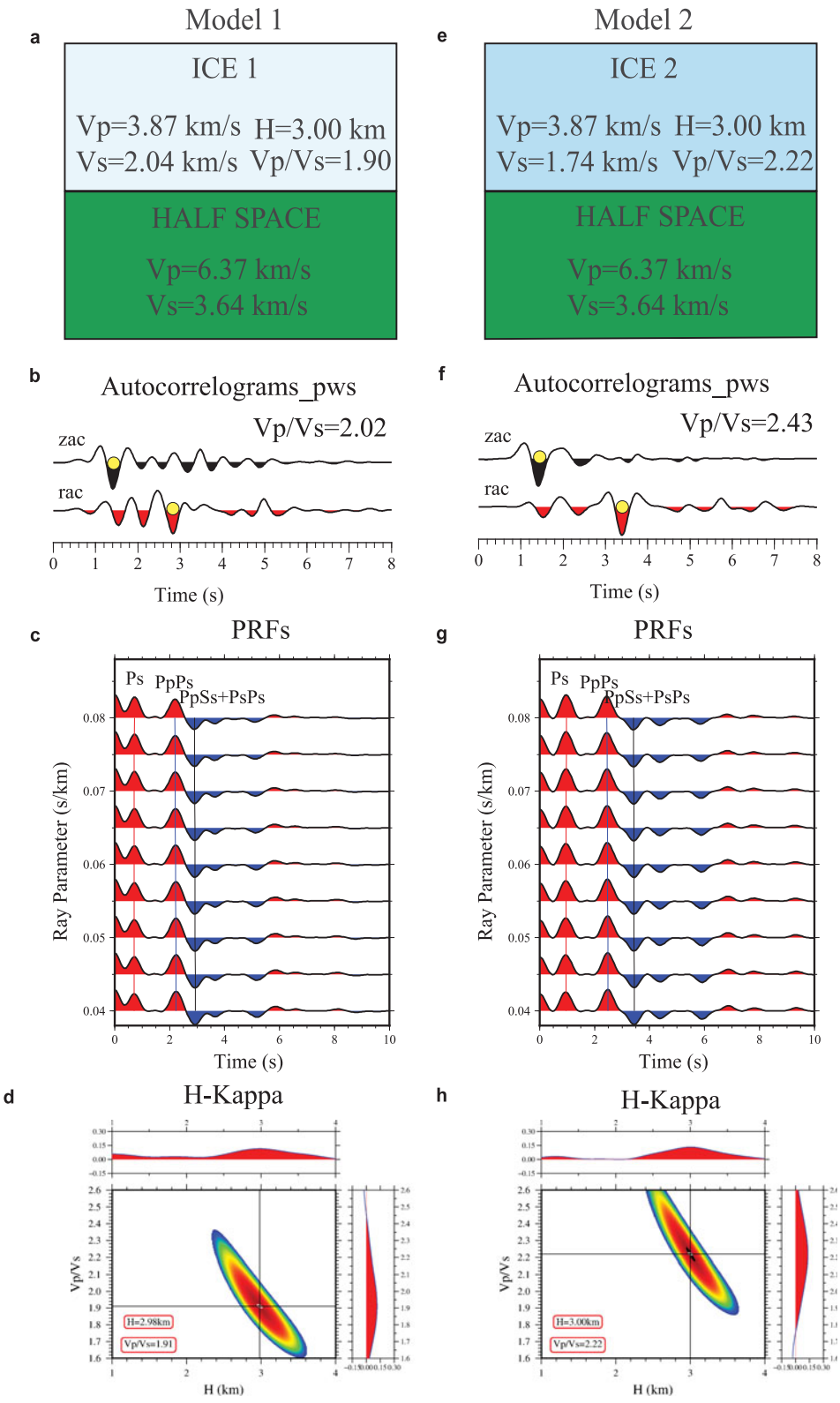

Fig. 7. Estimates of v_p/v_s ratios obtained from the PRF and autocorrelation methods using theoretical teleseimic waveforms based on models 1 and 2 (panels (a) and (e)). Panels (b), (c) and (d) show the stacked autocorrelograms, PRF waveforms and H-Kappa results for model 1, and the right panels display results for model 2. The arrival times used to calculate v_p/v_s ratios in panels (b) and (d) are automatically picked using the bootstrapping technique (Koch, 1992) shown in Fig. S14. The v_p/v_s ratio estimate obtained from PRF and H-Kappa methods is closer to the theoretical value than that measured using the autocorrelation method.

responses in ice, and in ice and sediment layers. $v_{P(s)}$ is P (S) wave velocities in ice, and $\bar{v}_{P(s)}$ is the weighted average P (S) wave velocities in ice and sediment layers. Figure 7 shows the results obtained from model 1 and model 2 assuming two ice-sheet layers with different values of v_p/v_s ratios. It is clear that the ice thickness and v_p/v_s ratio estimates obtained from the PRF and H-Kappa methods are closer to the theoretical values than those obtained from the autocorrelation method (Fig. 7). The deviations of the theoretical v_p/v_s ratios from the estimated ones are attributed to the differences between the theoretical and the observed P and S wave arrival times. For example, the theoretical P wave and S wave reflection arrival times of model 1 are 1.55 and 2.94 s, while the observed values are 1.4 and 2.83 s (Table S1). Figures 8 and S11 show that both the autocorrelograms and the PRF waveforms become complicated when sedimentary layers are involved. The H-Kappa technique failed to acquire optimum estimates of ice thickness and v_p/v_s ratios using PRF waveforms as the phases from the sediment-bedrock interface greatly obscure phases from the ice-sediment interface (Figs S11–S13). A comparison of the theoretical and the observed arrival times of P or

https://doi.org/10.1017/jog.2019.95 Published online by Cambridge University Press

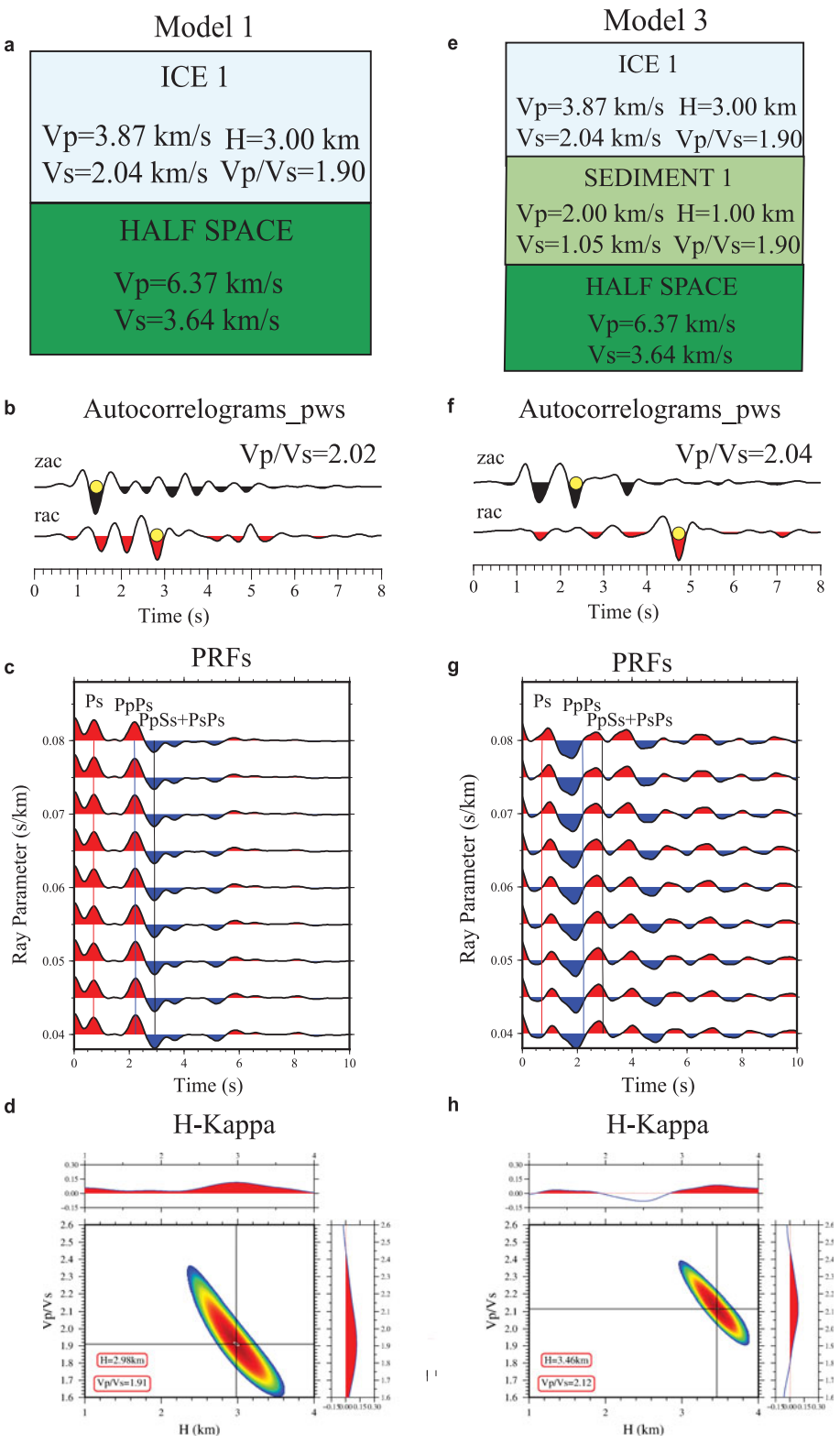

Fig. 8. Effect of a sediment layer (model 3) on v_p/v_s estimates obtained from the PRF and autocorrelation methods. Panels (b), (c) and (d) present the stacked autocorrelograms, PRF waveforms and the H-Kappa results for model 1, and the right panels show results for model 3. This comparison illustrates that neither the PRF method nor the autocorrelation method can clearly identify the ice-sediment interface (Table S1). The estimated v_p/v_s ratios obtained from the PRF and autocorrelation methods also deviate from the theoretical values.

S wave reflection responses indicates that the autocorrelation method can only identify interfaces associated with strong impedance contrasts (Table S1). For example, Figure S10 shows that the P wave impedance contrasts ($z = \rho \cdot v_p$, where z is the impedance contrast, and ρ and v_p are density and P wave velocity of the medium) set at the sediment-bedrock interfaces for models 4 and 6 are stronger than those set at the ice-sediment interfaces for models 3 and 5. Consequently, the observed P wave arrival times identified from models 3 (2.32 s) and 5 (2.35 s) are (nearly) equal to the theoretical times that were calculated with both the ice sheet and the sediment layers included (2.35 s for models 3 and 5). By contrast, the observed P wave arrival times of models 4 (1.46 s) and 6 (1.50 s) correspond to the theoretical times calculated with the single ice sheet layer (1.55 s). Similar results can be found for radial components (Table S1). Comparing results for models 3 and 4, we can find that the observed S wave arrival time of model 3 (4.73 s) is close to the theoretical arrival time (4.46 s) calculated including both the ice sheet and the sediment layers, while the observed arrival time of model 4 (2.77 s) approaches the theoretical arrival time (2.94 s) with the ice-sheet layer alone. We can also find that the observed S wave arrival time of model 6 (3.38 s) corresponds to the theoretical arrival time

https://doi.org/10.1017/jog.2019.95 Published online by Cambridge University Press

with the single ice-sheet layer (3.45 s) as the v_s value in ice decreases from 2.04 km s^{-1} in model 4 to 1.74 km s^{-1} in model 6, thus increasing the impedance contrast at the ice-sediment interface. Pham and Tkalčić (2018) pointed out that the low velocity of sediment results in low impedance contrast, explaining the relative transparency of sediment below an ice-sheet layer. In this sense, the autocorrelation method should be applied with caution to study low velocity sediment layers in glaciological settings. Alternatively, a nonlinear inversion method that is similar to the PRF waveform inversion approach could be effective to obtain the optimum model that fits with the observations.

The modeling results do not suggest that the autocorrelation method is superior to the PRF method, but it is still an effective alternative to the PRF method as it only requires a single component, which expands its application to datasets that were collected using single-component sensor decades ago. Moreover, the autocorrelation method can constrain both P wave and S wave velocity structures independently if both vertical and radial component records are available, while the PRF method can only reveal S wave velocity profiles. It is worth mentioning that there is a promising way to better constrain the thickness, v_p and v_s of an ice-sheet layer as a recent study has proposed a new H-Kappa-v_p stacking algorithm, which exploits independent constraints from the P wave autocorrelation and receiver functions (Delph and others, 2019).

Unlike the close relationship between the PRF and autocorrelation methods, there are more differences than similarities between the HVSR method and the autocorrelation method. First of all, seismic ambient noise data are usually adopted for HVSR processing, though earthquake records can also be used. Secondly, the spectrum peak observed by the HVSR method represents S wave resonance frequency and only reflects S wave energy trapped in a medium, while the autocorrelation method can reveal P and S wave energy separately. Both the autocorrelation and PRF methods require a certain number of teleseismic earthquakes, and such data usually take a relatively long time to collect in Antarctica. By contrast, the HVSR method applied to ambient noise records only requires a recording time of several hours, making it a valuable complement to the autocorrelation and PRF methods (Yan and others, 2018). Furthermore, the HVSR method combined with an inversion algorithm can be used to reveal inner stratification structures of ice sheets (Yan and others, 2018), which the autocorrelation method has failed to detect (Pham and Tkalčić, 2017).

As the v_p/v_s ratio is closely related to Poisson's ratio, we also calculated Poisson's ratio at each station using the relation shown in Eqn (10) (Christensen, 1996). The computed Poisson's ratios range from 0.32 to 0.38 (Table 1) and the average value (0.35) is slightly higher than the fixed value 0.33 used in previous studies (Gudmundsson, 2011; Rosier and others, 2015; Ramirez and others, 2016).

$$\upsilon = \frac{(v_p/v_s)^2 - 2}{2(v_p/v_s)^2 - 2} \tag{10}$$

Variations in the value of Poisson's ratio at different sites could be attributed to temperature differences in different regions. Thus, rather than using a constant value for Poisson's ratio, it is more reasonable to consider a variable Poisson's ratio for large-scale ice-sheet modeling.

5. Conclusions

Estimates of ice thickness and v_p/v_s ratios at 39 stations of the GAMSEIS and the ANET seismic arrays in Antarctica have been obtained using the recently proposed autocorrelation method. Results derived from the autocorrelation method were validated with synthetic tests at each station and compared with those derived from two other single-station passive seismic methods (i.e. the PRF and HVSR methods). The values of v_p/v_s ratios obtained in this study are within the range of experimental measurements. The spatial variations of elastic properties (e.g. Poisson's ratios deduced from v_p/v_s ratios) of ice sheets should be considered in large-scale modeling of ice-sheet dynamics. Consistent estimates of ice thickness are found among the PRF, HVSR and autocorrelation methods. Comparisons conducted under various model setups show the effectiveness of the autocorrelation method is not superior to the PRF method for retrieving seismic structures of ice sheets. However, the use of seismic records of a single component seismometer expands its application to datasets collected using only one-component sensors. It also opens a way to constrain P wave and S wave velocity profiles separately. However, in cases where the PRF and autocorrelation methods cannot be used due to a short time record of seismic data, the HVSR method can be a valuable tool for ice-sheet structure detection.

Acknowledgement. We thank the editor and reviewers for their constructive comments that greatly improved the manuscript. This work was supported by the State Key Program of National Natural Science of China under Grant 41531069, NSFC41476163, NSFC41674065, CAST-BISEE Foundation and the Chinese Polar Environment Comprehensive Investigation and Assessment Programs under Grant CHINARE2017-02-03. Seismic data used in this study are obtained from the Incorporated Research Institutions for Seismology (IRIS). Figures in this study were plotted using Generic Mapping Tools (GMT).

Supplementary material. The supplementary material for this article can be found at https://doi.org/10.1017/jog.2019.95

References

Anandakrishnan S and Winberry JP (2004) Antarctic subglacial sedimentary layer thickness from receiver function analysis. *Global and Planetary Change* **42**(1–4), 167–176. doi: 10.1016/j.gloplacha.2003.10.005.

Aster RC and Winberry JP (2017) Glacial seismology. *Reports on Progress in Physics* **80**, 126801. doi: 10.1088/1361-6633/aa8473.

Bamber JL, Layberry RL and Gogineni SP (2001) A new ice thickness and bed data set for the Greenland ice sheet: 1. Measurement, data reduction, and errors. *Journal of Geophysical Research: Atmospheres* **106**(D24), 33773–33780. doi: 10.1029/2001JD900054.

Bao F and 6 others (2018) Shallow structure of the Tangshan fault zone unveiled by dense seismic array and horizontal-to-vertical spectral ratio method. *Physics of the Earth and Planetary Interiors* **281**, 46–54. doi: 10.1016/j.pepi.2018.05.004.

Campillo M and Paul A (2003) Long-range correlations in the diffuse seismic coda. *Science* **299**(5606), 547–549. doi: 10.1126/science.1078551.

Chaput J and 5 others (2014) The crustal thickness of West Antarctica. *Journal of Geophysical Research: Solid Earth* **119**(1), 378–395. doi: 10.1002/2013JB010642.

Christensen NI (1996) Poisson's ratio and crustal seismology. *Journal of Geophysical Research: Solid Earth* **101**(B2), 3139–3156. doi: 10.1029/95jb03446.

Claerbout JF (1968) Synthesis of a layered medium from its acoustic transmission response. *Geophysics* **33**(2), 264–269. doi: 10.1190/1.1439927.

Clayton RW and Wiggins RA (1976) Source shape estimation and deconvolution of teleseismic bodywaves. *Geophysical Journal International* **47**(1), 151–177. doi: 10.1111/j.1365-246x.1976.tb01267.x.

Cuffey KM and Paterson WSB (2010) *The Physics of Glaciers*, 4th Edn. Oxford: Butterworth-Heinemann.

Delph JR, Levander A and Niu F (2019) Constraining crustal properties using receiver functions and the autocorrelation of earthquake-generated body waves. *Journal of Geophysical Research: Solid Earth* **124**(8), 8981–8997. doi: 10.1029/2019jb017929.

Diez A and 8 others (2016) Ice shelf structure derived from dispersion curve analysis of ambient seismic noise, Ross Ice Shelf, Antarctica. *Geophysical Journal International* **205**(2), 785–795. doi: 10.1093/gji/ggw036.

Drewry DJ, Jordan SR and Jankowski E (1982) Measured properties of the Antarctic ice sheet: surface configuration, ice thickness, volume and bedrock characteristics. *Annals of Glaciology* **3**, 83–91. doi: 10.3189/s0260305500002573.

Evans S and Robin GQ (1966) Glacier depth sounding from the air. *Nature* **210**, 883–885.

Frasier CW (1970) Discrete time solution of plane P-SV waves in a plane layered medium. *Geophysics* **35**(2), 197–219. doi: 10.1038/210883a0.

Fretwell P and 59 others (2013) Bedmap2: improved ice bed, surface and thickness datasets for Antarctica. *Cryosphere* **7**(1), 375–393. doi: 10.5194/tc-7-375-2013.

Gagliardini O and 14 others (2013) Capabilities and performance of Elmer/Ice, a new generation ice-sheet model. *Geoscientific Model Development* **6**(4), 1299–1318. doi: 10.5194/gmd-6-1299-2013.

Gagnon RE and 3 others (1988) Pressure dependence of the elastic constants of ice Ih to 2.8 kbar by Brillouin spectroscopy. *Journal of Chemical Physics* **89**(8), 4522–4528. doi: 10.1051/jphyscol:1987104.

Gogineni S (2001) Coherent radar ice thickness measurements over the Greenland ice sheet. *Journal of Geophysical Research: Atmospheres* **106** (D24), 33761–33772. doi: 10.1029/2001JD900183.

Gorbatov A, Saygin E and Kennett BLN (2012) Crustal properties from seismic station autocorrelograms. *Geophysical Journal International* **192**(2), 861–870. doi: 10.1093/gji/ggs064.

Gudmundsson GH (2011) Ice-stream response to ocean tides and the form of the basal sliding law. *Cryosphere* **5**(1), 259–270. doi: 10.5194/tc-5-259-2011.

Hanna E and 11 others (2013) Ice-sheet mass balance and climate change. *Nature* **498**(7452), 51. doi: 10.1038/nature12238.

Hansen SE and 5 others (2010) Crustal structure of the Gamburtsev Mountains, East Antarctica, from S-wave receiver functions and Rayleigh wave phase velocities. *Earth and Planetary Science Letters* **300**(3–4), 395–401. doi: 10.1016/j.epsl.2010.10.022.

Harland SR and 6 others (2013) Deformation in Rutford Ice Stream, West Antarctica: measuring shear-wave anisotropy from icequakes. *Annals of Glaciology* **54**(64), 105–114. doi: 10.3189/2013AoG64A033.

Horgan HJ and 4 others (2011) Englacial seismic reflectivity: imaging crystal-orientation fabric in West Antarctica. *Journal of Glaciology* **57**(204), 639–650. doi: 10.3189/002214311797409686.

Kennett BLN (2015) Lithosphere–asthenosphere P-wave reflectivity across Australia. *Earth and Planetary Science Letters* **431**, 225–235. doi: 10.1016/j.epsl.2015.09.039.

Kennett BLN, Saygin E and Salmon M (2015) Stacking autocorrelograms to map Moho depth with high spatial resolution in southeastern Australia. *Geophysical Research Letters* **42**(18), 7490–7497. doi: 10.1002/2015GL065345.

Kim KY and 5 others (2010) Seismic and radar investigations of Fourcade Glacier on King George Island, Antarctica. *Polar Research* **29**(3), 298–310. doi: 10.3402/polar.v29i3.6082.

Koch M (1992) Bootstrap inversion for vertical and lateral variations of the S wave structure and the υ_p/υ_s-ratio from shallow earthquakes in the Rhinegraben seismic zone, Germany. *Tectonophys* **210**(1–2), 91–115. doi: 10.1016/0040-1951(92)90130-X.

Köhler A and Weidle C (2019). Potentials and pitfalls of permafrost active layer monitoring using the HVSR method: a case study in Svalbard. *Earth Surface Dynamics* **7**(1), 1–16. doi: 10.5194/esurf-7-1-2019.

Kohnen H (1974). The temperature dependence of seismic waves in ice. *Journal of Glaciology* **13**(67), 144–147. doi: 10.3189/S0022143000023467.

Langston CA (1979) Structure under Mount Rainier, Washington, inferred from teleseismic body waves. *Journal of Geophysical Research* **84**, 4749–4762. doi: 10.1029/JB084iB09p04749.

Lévêque JJ, Maggi A and Souriau A (2010) Seismological constraints on ice properties at Dome C, Antarctica, from horizontal to vertical spectral ratios. *Antarctic Science* **22**(5), 572–579. doi: 10.1017/S0954102010000325.

Li J and 8 others (2013) High-altitude radar measurements of ice thickness over the Antarctic and Greenland ice sheets as a part of operation icebridge. *IEEE Transactions on Geoscience and Remote Sensing* **51**(2), 742–754. doi: 10.1109/TGRS.2012.2203822.

Li Z and 6 others (2016) Shallow magma chamber under the Wudalianchi volcanic field unveiled by seismic imaging with dense array. *Geophysical Research Letters* **43**(10), 4954–4961. doi: 10.1002/2016GL068895.

Lunedei E and Malischewsky P (2015) A review and some new issues on the theory of the H/V technique for ambient vibrations. In Ansal A ed. *Perspectives on European Earthquake Engineering and Seismology*. Springer, Cham, 371–394. doi: 10.1007/978-3-319-16964-4_15.

Lythe MB and Vaughan DG (2001) BEDMAP: a new ice thickness and subglacial topographic model of Antarctica. *Journal of Geophysical Research: Solid Earth* **106**(B6), 11335–11351. doi: 10.1029/2000JB900449.

Nakamura Y (1989) A method for dynamic characteristics estimation of subsurface using microtremor on the ground surface. *Quarterly Report of the Railway Technical Research Institute* **30**(1), 25–30.

Nishitsuji Y and 3 others (2016) Reflection imaging of the Moon's interior using deep-moonquake seismic interferometry. *Journal of Geophysical Research: Planets***121**(4), 695–713. doi: 10.1002/2015JE004975.

Phạm TS and Tkalčić H (2017) On the feasibility and use of teleseismic P wave coda autocorrelation for mapping shallow seismic discontinuities. *Journal of Geophysical Research: Solid Earth* **122**(5), 3776–3791. doi: 10.1002/2017JB013975.

Phạm TS and Tkalčić H (2018) Antarctic ice properties revealed from teleseismic P wave coda autocorrelation. *Journal of Geophysical Research: Solid Earth* **123**(9), 7896–7912. doi: 10.1029/2018JB016115.

Picotti S and 4 others (2015) Anisotropy and crystalline fabric of Whillans Ice Stream (West Antarctica) inferred from multicomponent seismic data. *Journal of Geophysical Research: Solid Earth* **120**(6): 4237–4262. doi: 10.1002/2014JB011591.

Picotti S and 4 others (2017) Estimation of glacier thicknesses and basal properties using the horizontal-to-vertical component spectral ratio (HVSR) technique from passive seismic data. *Journal of Glaciology* **63**(238), 229–248. doi: 10.1017/jog.2016.135.

Podolskiy EA and Walter F (2016) Cryoseismology. *Reviews of Geophysics* **54**(4), 708–758. doi: 10.1002/2016RG000526.

Preiswerk LE and 3 others (2019) Effects of geometry on the seismic wavefield of Alpine glaciers. *Annals of Glaciology* **60**(79), 112–124. doi: 10.1017/aog.2018.27.

Ramirez C and 8 others (2016) Crustal and upper-mantle structure beneath ice-covered regions in Antarctica from S-wave receiver functions and implications for heat flow. *Geophysical Journal International* **204**(3), 1636–1648. doi: 10.1093/gji/ggv542.

Randall GE (1989) Efficient calculation of differential seismograms for lithospheric receiver functions. *Geophysical Journal International* **99**(3), 469–481. doi: 10.1111/j.1365-246X.1989.tb02033.x.

Robinson ES (1968) Seismic wave propagation on a heterogeneous polar ice sheet. *Journal of Geophysical Research* **73**(2), 739–753. doi: 10.1029/JB073i002p00739.

Rosier SH, Gudmundsson GH and Green JM (2015) Temporal variations in the flow of a large Antarctic ice stream controlled by tidally induced changes in the subglacial water system. *Cryosphere* **9**(4), 1649–1661. doi: 10.5194/tc-9-1649-2015.

Röthlisberger H (1972) *Seismic Exploration in Cold Regions*. Cold Regions Research and Engineering Laboratory, Hanover, NH.

Saygin E, Cummins PR and Lumley D (2017) Retrieval of the P wave reflectivity response from autocorrelation of seismic noise: Jakarta Basin, Indonesia. *Geophysical Research Letters* **44**(2), 792–799. doi: 10.1002/2016GL071363.

Schimmel M and Gallart J (2007) Frequency-dependent phase coherence for noise suppression in seismic array data. *Journal of Geophysical Research: Solid Earth* **112**(B4). doi: 10.1029/2006JB004680.

Shapiro NM and Campillo M (2004) Emergence of broadband Rayleigh waves from correlations of the ambient seismic noise. *Geophysical Research Letters* **31**(7). doi: 10.1029/2004GL019491.

Smith EC and 6 others (2017) Ice fabric in an Antarctic ice stream interpreted from seismic anisotropy. *Geophysical Research Letters* **44**(8), 3710–3718. doi: 10.1002/2016GL072093.

Sun W and Kennett BLN (2016) Receiver structure from teleseisms: autocorrelation and cross correlation. *Geophysical Research Letters* **43**(12), 6234–6242. doi: 10.1002/2016GL069564.

Sun W and Kennett BLN (2017) Mid-lithosphere discontinuities beneath the western and central North China Craton. *Geophysical Research Letters* **44** (3), 1302–1310. doi: 10.1002/2016GL071840.

Tibuleac IM and von Seggern D (2012) Crust-mantle boundary reflectors in Nevada from ambient seismic noise autocorrelations. *Geophysical Journal International* **189**(1), 493–500. doi: 10.1111/j.1365-246X.2011.05336.x.

Walter F and 5 others (2015) Using glacier seismicity for phase velocity measurements and Green's function retrieval. *Geophysical Journal International* **201**(3), 1722–1737. doi: 10.1093/gji/ggv069.

Walter F, Chaput J and Lüthi MP (2014) Thick sediments beneath Greenland's ablation zone and their potential role in future ice sheet dynamics. *Geology* **42**(6), 487–490. doi: 10.1130/G35492.1.

Wapenaar K, Thorbecke J and Draganov D (2004) Relations between reflection and transmission responses of three-dimensional inhomogeneous media. *Geophysical Journal International* **156**(2), 179–194. doi: 10.1111/j.1365-246X.2003.02152.x.

https://doi.org/10.1017/jog.2019.95 Published online by Cambridge University Press

Wittlinger G and Farra V (2012) Observation of low shear wave velocity at the base of the polar ice sheets: evidence for enhanced anisotropy. *Geophysical Journal International* **190**(1), 391–405. doi: 10.1111/j.1365-246X.2012.05474.x.

Wittlinger G and Farra V (2015) Evidence of unfrozen liquids and seismic anisotropy at the base of the polar ice sheets. *Polar Science* **9**(1), 66–79. doi: 10.1016/j.polar.2014.07.006.

Yan P and 5 others (2017) Antarctic ice sheet thickness derived from teleseismic receiver functions. *Chinese Journal of Geophysics* **60**(10), 3780–3792. doi: 10.6038/cjg20171008.

Yan P and 5 others (2018) Antarctic ice sheet thickness estimation using the horizontal-to-vertical spectral ratio method with single-station seismic ambient noise. *Cryosphere* **12**(2), 795–810. doi: 10.5194/tc-12-795-2018.

Zhan Z and 3 others (2014) Ambient noise correlation on the Amery Ice Shelf, east Antarctica. *Geophysical Journal International* **196**(3), 1796–1802. doi: 10.1093/gji/ggt488.

Zhu L and Kanamori H (2000) Moho depth variation in Southern California from Teleseismic receiver functions. *Journal of Geophysical Research: Solid Earth* **105**(B2), 2969–2980. doi: 10.1029/1999JB900322.

https://doi.org/10.1017/jog.2019.95 Published online by Cambridge University Press